coatings

MDPI

Article

Design and Fabrication of Temperature-Compensated Film Bulk Acoustic Resonator Filter Based on the Stress Compensation Effect

Ya Liu [1,2,*], Ke Sun [1,*], Jinyi Ma [2], Zhong Yu [1] and Zhongwen Lan [1]

[1] School of Materials and Energy, University of Electronic Science and Technology of China, Chengdu 610054, China
[2] 26th Institute of China Electronics Technology Group Corporation, Chongqing 400060, China
* Correspondence: liuya_26@163.com (Y.L.); ksun@uestc.edu.cn (K.S.)

Abstract: To ensure that the performance of filters matches the continuous development in communication frequency bands, the influence of temperature on filter performance must be considered during the fabrication of filters. In this study, a cavity-type temperature-compensated film bulk acoustic resonator (TC-FBAR) device was prepared with an SiO_2 temperature filter between the bottom electrode and the piezoelectric layer. A one-dimensional Mason model of the TC-FBAR was established. An advanced design system, a high-frequency structure simulator, and COMSOL software were used to optimize the design of the TC-FBAR. After the optimization, the out-of-band rejection was improved by 10 dB. To address the compensation effect of the tensile and compressive stresses, a multilayer film was implemented for low-stress control and a reduction in stress to $|P| \leq 150$ MPa, thereby improving the orientation of the piezoelectric film. Moreover, the influence of the thickness of the SiO_2 temperature-compensated layers on the temperature-compensated characteristics was studied. When the SiO_2 thickness was 50 nm, the temperature coefficient of frequency (*TCF*) was ±1 ppm/°C. The center frequency and 3 dB bandwidth of TC-FBAR were 2.492 GHz and 15.02 MHz, respectively, and the center insertion loss was −3.1 dB. Moreover, the out-of-band rejection was greater than 40 dBc, and *TCF* was 0.8 ppm/°C.

Keywords: temperature-compensated film bulk acoustic resonator; Mason model; composite film; temperature-compensated layer; temperature coefficient of frequency

check for updates

Citation: Liu, Y.; Sun, K.; Ma, J.; Yu, Z.; Lan, Z. Design and Fabrication of Temperature-Compensated Film Bulk Acoustic Resonator Filter Based on the Stress Compensation Effect. *Coatings* **2022**, *12*, 1126. https://doi.org/10.3390/coatings12081126

Academic Editor: Alessio Lamperti

Received: 23 June 2022
Accepted: 2 August 2022
Published: 5 August 2022

1. Introduction

With the rapid development of electronic equipment systems and mobile communication technology, communication frequency bands (S and C bands) are further extended to higher frequencies. Consequently, phased-array radars, electronic countermeasures, and communication systems have increasingly high requirements for the temperature coefficient of frequency (*TCF*), performance, and volume of high-frequency filters [1–3]. Further, the increased scarcity of communication spectrum resources complicates the frequency band allocation and narrows the protection frequency band with more stringent market requirements on filter performance.

The film bulk acoustic resonator (FBAR) filter is a key component in radio frequency (RF) systems. In particular, every RF signal and communication frequency band uses filters to suppress interference signals. Thus, filters play a vital role in the control of electromagnetic power. As FBARs have a large *TCF* [4–8], the device performance in the entire temperature range should be considered in the filter design. As the *TCF* increases, the filter bandwidth widens to more than the required bandwidth, resulting in a more difficult design. The resonant frequency (f) of the FBAR is determined by the thickness (d) and the longitudinal wave velocity (v) of the volume acoustic wave propagating in the resonator, v as follows:

$$f = v/d \tag{1}$$

$$v = \sqrt{E/\rho} \tag{2}$$

where E is the Young's modulus of the material, and ρ is the density of the material [9,10].

For AlN and Mo, the Young's modulus decreases with increasing temperature [11–14]. The *TCF* of conventional Mo–AlN–Mo-structured FBAR is approximately −30 ppm/°C [15]. As a commonly used semiconductor material, the Young's modulus of SiO_2 increases with the increase of temperature, achieving a *TCF* of +85 ppm/°C [16,17]; thus, SiO_2 can be used as the temperature-compensated material for FBARs. By increasing the thickness of the SiO_2 temperature-compensated layer, which has a positive *TCF* [18], and using the principle of mutually compensated materials with positive and negative *TCF*s, the *TCF* of FBARs can be controlled at a low value; however, the insertion loss increases with the addition of SiO_2. In particular, using a ZnO micromachined cantilever as the piezoelectric layer and SiO_2 as the temperature-compensated layer, a *TCF* of −0.45 ppm/°C can be achieved [19]. However, the micromachined cantilever has low reliability and is prone to fracture. Moreover, ZnO is not compatible with semiconductor processing. When a small modular reactor (SMR) filter adopts SiO_2 as the temperature-compensated layer, the *TCF* can reach 1 ppm/°C [20,21]. However, SMRs require a highly precise film thickness. After doping fluorine in SiO_2 as the temperature-compensated layer, the electromechanical coupling coefficient ($k^2{}_t$) can be increased to 6.26%, and a *TCF* of −11.1 ppm/°C can be achieved [22]. Meanwhile, after doping boron in SiO_2 as the temperature-compensated layer, a *TCF* of up to −1.5 ppm/°C was obtained with an improved quality factor (*Q*) value [23]. Thus, the doped SiO_2 temperature-compensated layer is suitable for the production of broadband filters. However, this process is relatively complex, and requires the use of expensive equipment.

Thus, in this study, based on the conventional Mason model, a Mason model of the temperature-compensated FBAR (TC-FBAR) was established, and the resonator and filter were co-simulated and optimized by COMSOL, a high-frequency structure simulator (HFSS), and an advanced design system (ADS). Further, a method for preparing the cavity structure of a low-stress multilayer composite film was adopted to incorporate an SiO_2 temperature-compensated layer between the bottom electrode and the piezoelectric layer. The proposed method can obtain piezoelectric thin films with the preferred orientation as well as fabricate filters with a low insertion loss, a narrow bandwidth, a high out-of-band rejection, and a low *TCF* that meet the requirements of a low-temperature drift narrowband filter.

2. Materials and Methods

2.1. Design of the FBAR Filter

2.1.1. FBAR Model

According to Mason's equivalent model in the traditional piezoelectric theory [24], the equivalent circuit of the piezoelectric and acoustic layers was cascaded to obtain the traditional FBAR equivalent circuit. From the traditional FBAR Mason model, the equivalent circuits of the adhesion and temperature-compensated layers were added to obtain a Mason model of the TC-FBAR, as shown in Figure 1a. A finite element analysis (FEA) based on COMSOL Multiphysics software was performed using the TC-FBAR Mason model structure, as shown in Figure 1b.

2.1.2. Design of TC-FBAR

A three-dimensional electromagnetic model of the package, a die pad, and a wire bonding line was established in a HFSS. The size, position, and thickness of the pad, and the number and position of the wire bonding lines were optimized, thereby optimizing the near and outer ends of the out-of-band filter. From the FEA, the peripheral electromagnetic environmental parameters of TC-FBAR were obtained, as shown in Figure 2a.

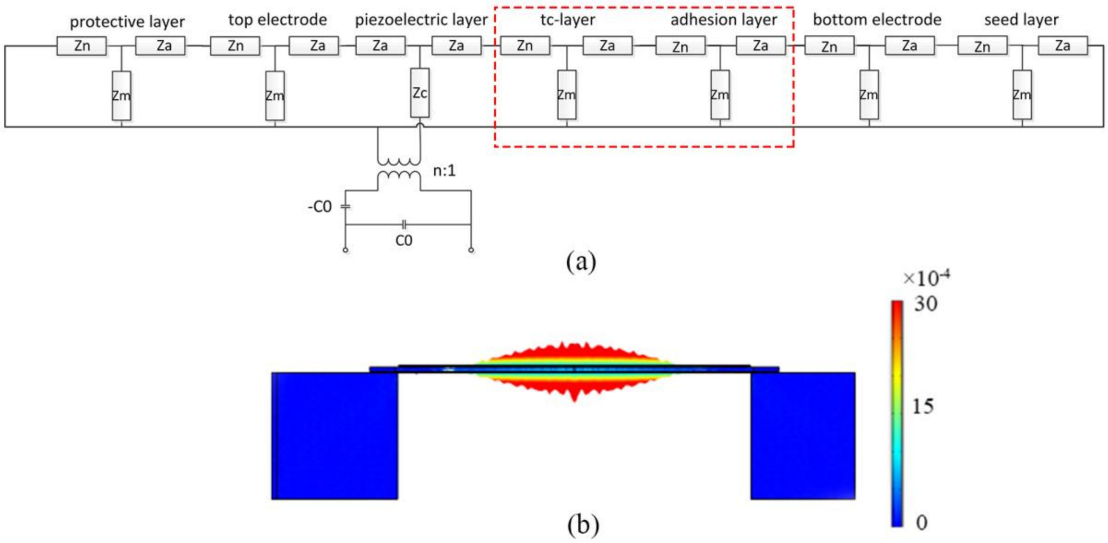

Figure 1. (**a**) Mason model of the TC-FBAR. (**b**) Simulated displacement field at the resonant frequency of TC-FBAR.

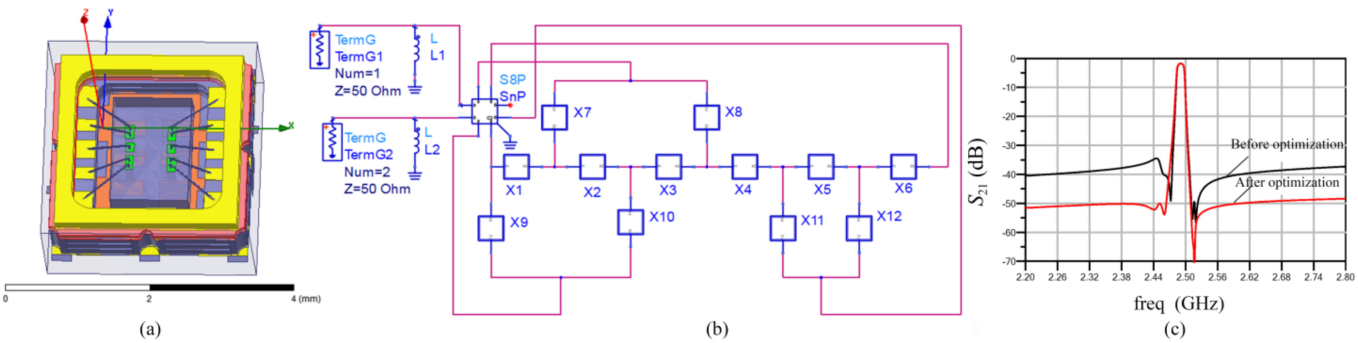

Figure 2. (**a**) HFSS model. (**b**) TC-FBAR full-wave simulation diagram. (**c**) Performance comparison after the simulation optimization.

The peripheral electromagnetic parameters and resonator model obtained by the HFSS and, subsequently, the lumped parameter matching circuit were imported into the ADS. The optimized design of the device was realized through the optimization algorithm in ADS. The topological structure adopted six series and six shunts, as shown in Figure 2b. This structure can address the problems of narrow bandwidth, high out-of-band rejection, and low insertion loss filters. In COMSOL, the resonator film thickness structure was optimized to ensure that it was in its optimal matching state, thereby reducing the insertion loss and improving the Q and $k^2{}_{eff}$. Q_s and Q_p are computed as follows:

$$Q_s = f_s / \Delta f_s \tag{3}$$

$$Q_p = f_p / \Delta f_p \tag{4}$$

where Δf_s and Δf_p are the -3 dB frequency widths of the impedance response $|Z|$ at f_s and f_p, respectively. The effective coupling coefficient $k^2{}_{eff}$ is derived from the series resonant frequency f_s and parallel resonance frequency f_p [22] as follows:

$$k^2{}_{eff} = (\pi^2/4)(f_s/f_p)[(f_p - f_s)/f_p] \tag{5}$$

In the HFSS, the layout of the resonators and the number and position of wire bonding were optimized to reduce the electromagnetic parasitic effect and inductance as well as improve the out-of-band rejection. In ADS, filters with low loss and high out-of-band suppression were obtained by optimizing the topology, number, and size of the resonators, as well as the series–parallel mode. The simulation performance diagram after optimization is shown in Figure 2c. After optimization, the out-of-band rejection was 50 dB, which was 10 dB higher than that before optimization.

2.2. Film Fabrication

In this study, a high-resistance silicon wafer (resistivity of >5000 Ω·cm) and SiO_2 films were used as the temperature-compensated layer to produce the TC-FBAR filter. The fabrication process is shown in Figure 3. Owing to the introduction of the SiO_2 temperature-compensated layer, the upper and lower film layers were prepared using different methods and physical parameters. This resulted in difficulties in controlling the stress, easy separation of the components [25], widened full width at half-maximum (FWHM), and other phenomena that seriously affect the device performance or even cause failure of the composite film. Therefore, the preparation of the temperature-compensated composite film is a key technology in TC-FBAR.

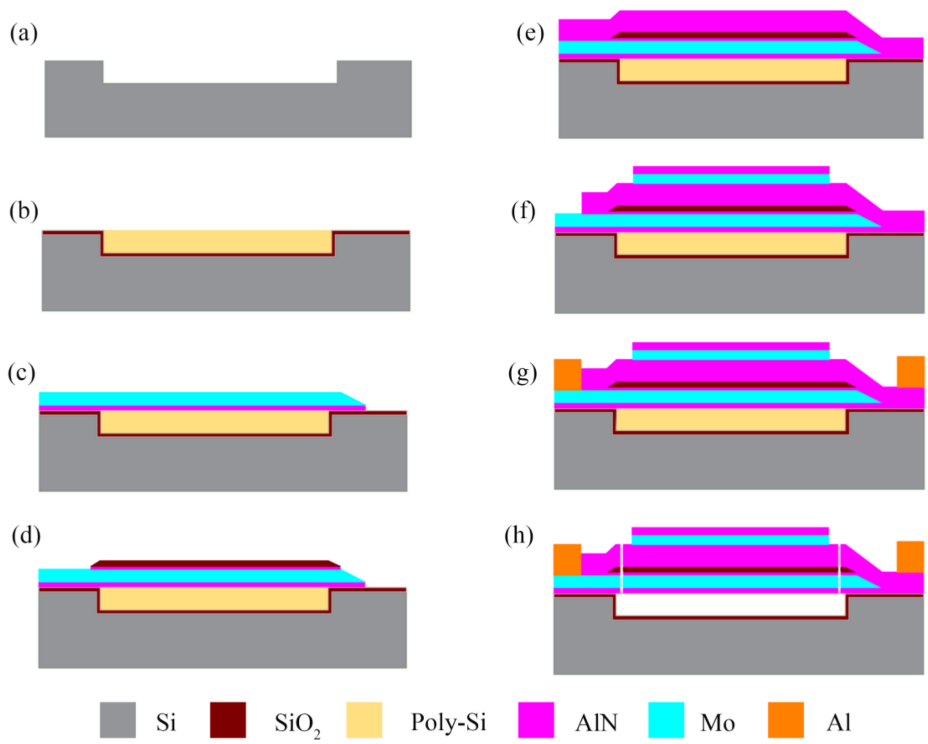

Figure 3. Fabrication process of the TC-FBAR: (**a**) silicon etching; (**b**) thermal oxidation and poly-Si deposition and chemical mechanical polishing; (**c**) AlN seed layer and Mo deposition and etching; (**d**) adhesion layer AlN and SiO_2 temperature-compensated layer deposition and etching; (**e**) piezoelectric layer and AlN deposition; (**f**) top Mo and AlN protective layer deposition and etching; (**g**) Al pad formation; (**h**) AlN etching and polysilicon release.

2.2.1. SiO_2 Film Fabrication

Plasma-enhanced chemical vapor deposition method was used to prepare the SiO_2 films [26,27]. The film thickness was adjusted using the growth time. The growth of a substrate layer, such as Ti or AlN, before SiO_2 deposition can improve adhesion during SiO_2 growth, which can prevent the fall off of the SiO_2 film.

2.2.2. Mo Electrode Film Fabrication

The Mo electrode thin film was prepared by direct current (DC) magnetron sputtering. By adjusting the sputtering power and argon flow rate [28], the stress of the Mo film in the electrode layer can be adjusted to 0 and 100 MPa, as shown in Figure 4a. The process parameters of the Mo film growth are as follows: alternating current (AC) power, DC power, RF power, and Ar flow rate of 0.5 kW, 3 kW, 35 W, and 60 sccm, respectively. In addition to optimizing the process parameters during Mo sputtering, an AlN seed layer was grown before the deposition of the Mo electrode, which greatly improved its orientation. To improve the induction effect of the seed layer, the substrate support layer was pretreated before growing the seed layer, and the support layer on the substrate was dusted with argon plasma to activate it and improve the preferred orientation of the Mo film. The FWHM of Mo's (110) swing curve was reduced from 2.0197° to 1.6164° after optimization, as shown in Figure 4b. The surface, as evidenced by the increased intensity of the peak, indicated a higher degree of crystallization. The FWHM of the Mo films largely depends on the orientation and surface roughness of the substrate. The roughness of the Mo films prepared by DC magnetron sputtering was 0.294 nm, as shown in Figure 4c, which satisfies the process requirements. Moreover, the film surface is dense, smooth, and evenly distributed with few protrusions.

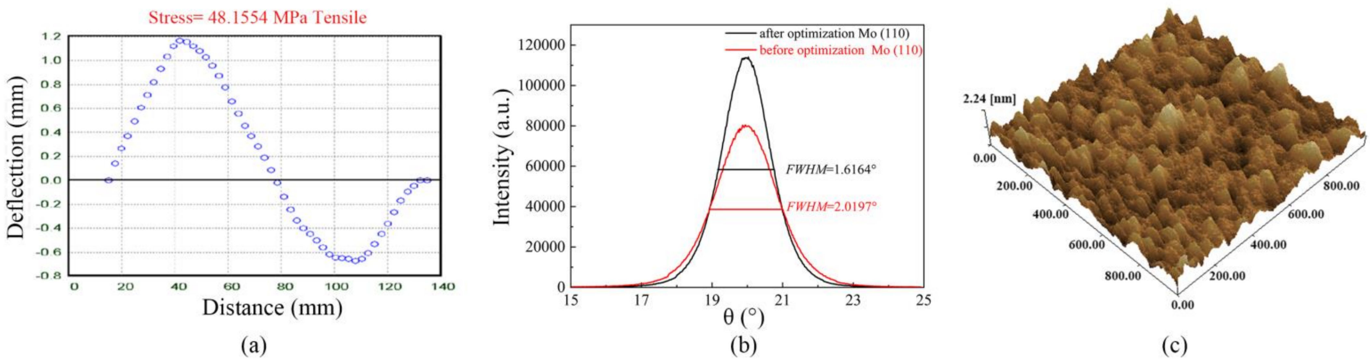

Figure 4. (**a**) Stress diagram of the bottom electrode of Mo. (**b**) Swing curve of Mo (110). (**c**) Surface roughness of the Mo film.

To avoid defects, such as poor coverage of the upper film, poor orientation, and excessive stress at the step, due to the excessive angle after etching the bottom electrode, a bottom electrode step with a smaller angle was obtained by adjusting the process parameters [29], as shown in Figure 5. An angle of 13.23° was used to ensure the growth quality of the upper film.

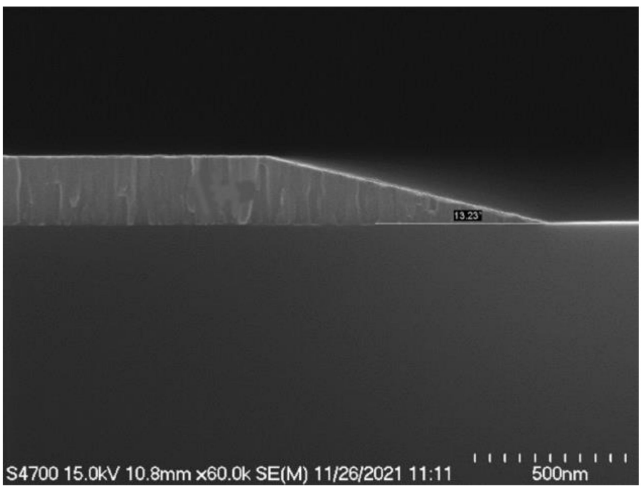

Figure 5. Small-angle diagram after etching the bottom electrode.

2.2.3. AlN Piezoelectric Film Fabrication

The AlN films were prepared on composite films, i.e., SiO_2 film passivation layer, sacrificial polysilicon film layer, AlN-supporting layer, Mo bottom electrode, and SiO_2 film temperature-compensated layer, by growing on a silicon substrate. Owing to the influence of stress accumulation and surface roughness, the preferred-orientation growth of the AlN film was more difficult than the direct growth of the AlN film on a silicon substrate. Thus, AlN film is mainly produced by magnetron sputtering [30,31]. In this study, the AlN film was prepared by intermediate frequency AC magnetron sputtering. The stress of the AlN film was adjusted by controlling the flow rate of the argon gas and through a stress-regulating resistance. The thin film stress measurement system was used to measure the stress of the thin film on the wafer before the growth of the AlN film. The stress of the AlN film was adjusted by preparing the multilayer film. If the composite film exhibited compressive stress, the AlN film was adjusted to exhibit tensile stress to achieve low stress for the film. The process growth parameters of the AlN film are as follows: AC power, DC power, RF power, Ar flow rate, and N_2 flow rate of 9 kW, 10 kW, 50 W, 60 sccm, and 45 sccm, respectively. The orientation of the AlN thin films was improved by RF plasma cleaning before AlN film plating. During the RF plasma cleaning, argon ions bombarded the substrate to remove water vapor and other adjacent crops on the substrate surface, which increased the mobility of the particles on the substrate surface and, consequently, improved the crystallization orientation of the AlN film. For the tensile and compressive stress compensation effects, the bottom electrode, temperature-compensated, and piezoelectric layers under stress, and roughness of the monolayer film were adjusted to decrease the stress of the multilayer piezoelectric composite film.

3. Results and Discussion

The roughness of the film was tested by atomic force microscopy (AFM). The roughness of the SiO_2 films with different thicknesses is shown in Figure 6. With the increase in the SiO_2 thickness, the roughness of the films gradually increases, which affects their quality. In particular, an excessively high roughness causes energy loss of the film surface, thereby increasing device loss [32]. Moreover, roughness affects the internal stress of the film, which is controlled by adjusting the process parameters, such as gas flow rate, power, and temperature.

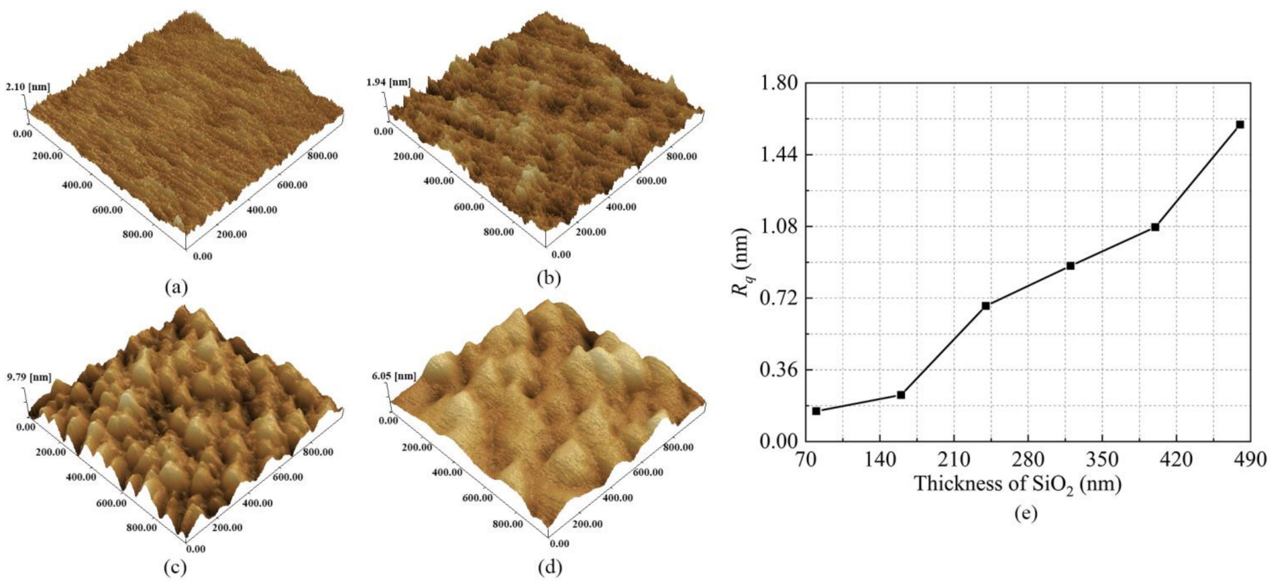

Figure 6. Roughness of the SiO_2 films of different thicknesses: (**a**) 80, (**b**) 160, (**c**) 240, and (**d**) 320 nm. (**e**) Surface roughness with different SiO_2 thicknesses.

The stress of the film was tested by the stress tester. The stress of the SiO_2 films with different thicknesses is shown in Figure 7. As the SiO_2 film thickness was increased, the stress gradually decreased. Moreover, a transformation from compressive to tensile stress was noted. This is ascribed to the lower deposition temperature in the films with a smaller thickness, which allows the escape of the reaction by-products as disordered substances in the film [33,34]. Thus, with the increase of the film thickness, the temperature of the film increased gradually due to the heat energy accumulation effect, it decreased the number of residual by-products in the film with accelerated escape, and transformed the stress from compressive to tensile stress. In addition, the (002) orientation of AlN is affected by the high stress, which can result in device film cracking or collapse after release. Thus, to improve the quality of the thin film and AlN (002) preferred orientation, a single-layer film was adopted to address the tensile- and compressive-stress-compensated effects, thereby realizing the low-stress control of the multilayer composite film. A schematic of the stress-compensated effect is shown in Figure 8. When the lower film exhibited compressive stress, the stress of the upper film was adjusted to the tensile stress to eliminate the stress of the composite film.

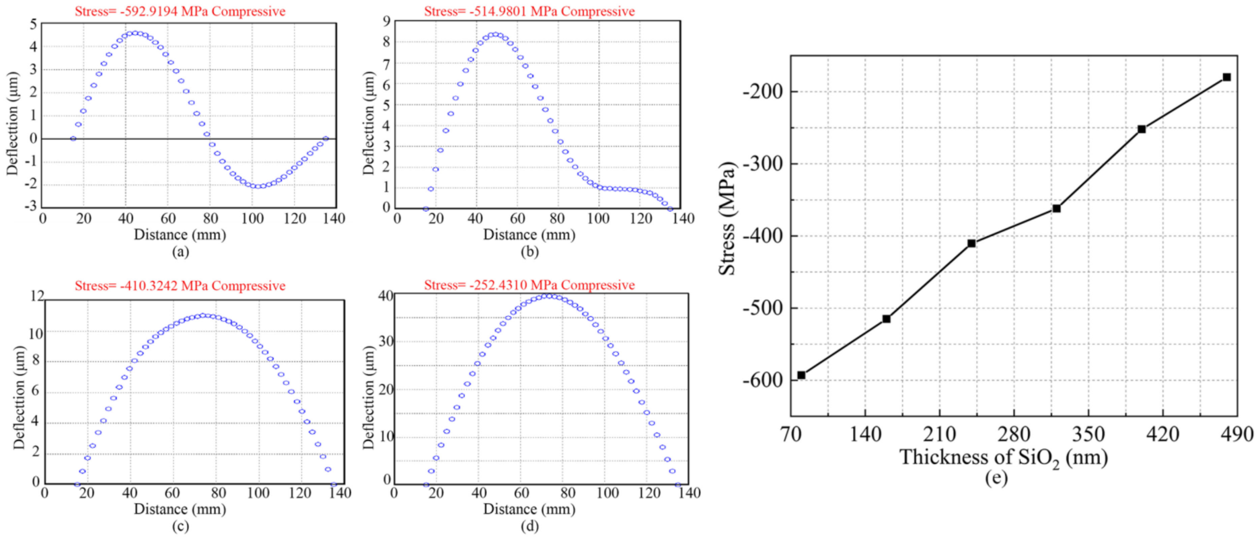

Figure 7. Stress of the SiO_2 films with different thicknesses: (**a**) 80, (**b**) 160, (**c**) 240, and (**d**) 320 nm. (**e**) Stress with different SiO_2 thicknesses.

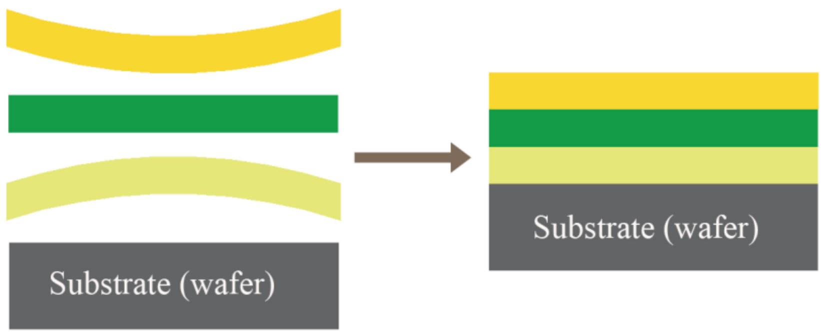

Figure 8. Schematic of the stress-compensated effect.

The X-ray diffraction (XRD) (002) orientation swing curve of the AlN film is shown in Figure 9. The FWHM of the AlN (002) swing curve was reduced from 2.361° to 1.885° after optimization, and the surface had a high peak strength, indicating the c-axis orientation and good crystallization of the AlN film [35–37].

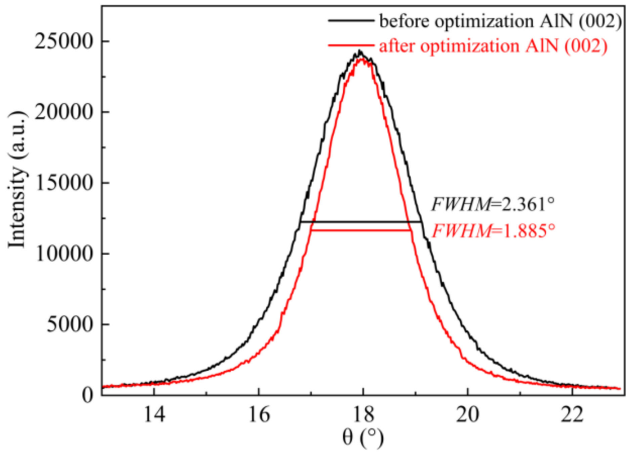

Figure 9. Swing curve of the AlN thin film.

The stress of the composite film was tested by the stress tester. The stress in the multilayer composite film is shown in Figure 10. By comparing the stress of the composite film before and after optimization, the stress (|P|) generated by the multilayer composite film was reduced from 800 to 150 MPa after optimization, thereby achieving the low-stress growth of the composite film.

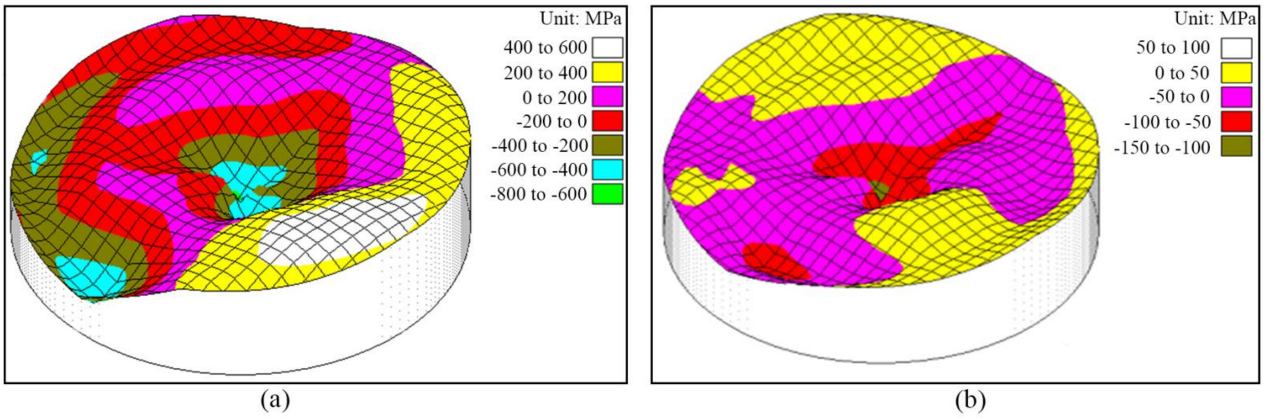

Figure 10. Three-dimensional stress diagram of the composite film: (**a**) before optimization, (**b**) after optimization.

A high-resistance silicon wafer and a cavity-type structure were used to fabricate the TC-FBAR filter. The appearance of the device was observed by a microscope, and the microstructure and membrane structure of the device were analyzed with transmission electron microscopy (TEM). The top view and TEM diagram of the TC-FBAR structure are shown in Figure 11. The layers exhibit good growth quality and adhesion, as shown in Figure 11b. The temperature-compensated characteristics of the temperature-compensated layers of different thicknesses were tested, as shown in Figure 12. As the thickness of the SiO_2 temperature-compensated layer gradually increased, the *TCF* changed from negative to positive, and gradually increased because of the positive *TCF* of SiO_2 and the negative *TCF* of the FBAR, as shown in Figure 12a. When the thickness of the temperature-compensated layer was approximately 50 nm, the *TCF* was ±1 ppm/°C, k^2_{eff} gradually decreased because the difference between f_p and f_s decreased gradually [38–40], and the corresponding bandwidth of the filter became narrower. As SiO_2 was added between the piezoelectric layer and bottom electrode, the piezoelectric performance of the piezoelectric layer was affected when the piezoelectric property was converted into electrical energy; thus, the piezoelectric property cannot be completely converted into electrical energy, thereby reducing the effective coupling coefficient. The *Q* decreased gradually with an increase in the thickness of the temperature-compensated layer, because the acoustic energy was lost after adding SiO_2, and −3 dB frequency widths were increased.

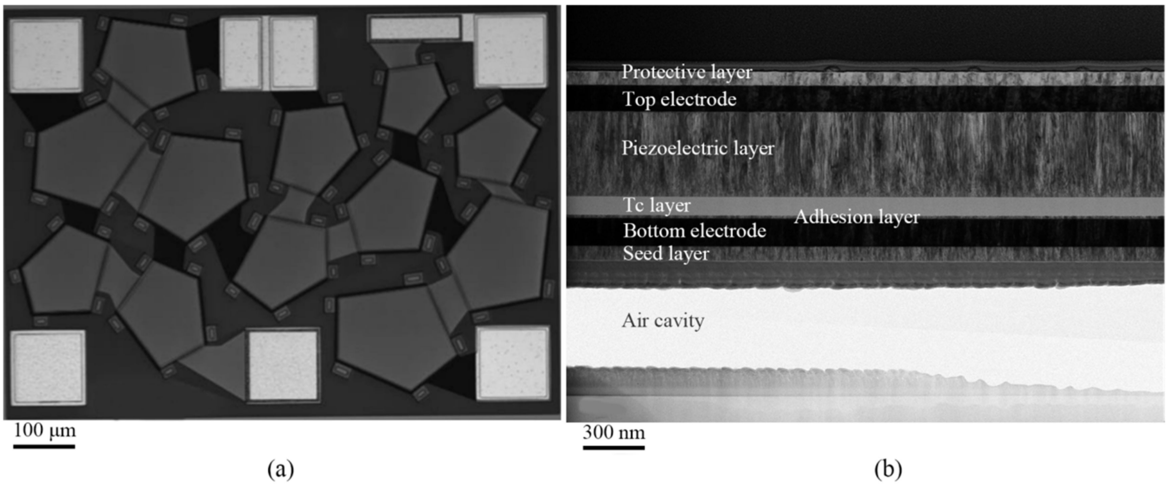

Figure 11. (**a**) Top view of the TC-FBAR. (**b**) TEM diagram of the TC-FBAR.

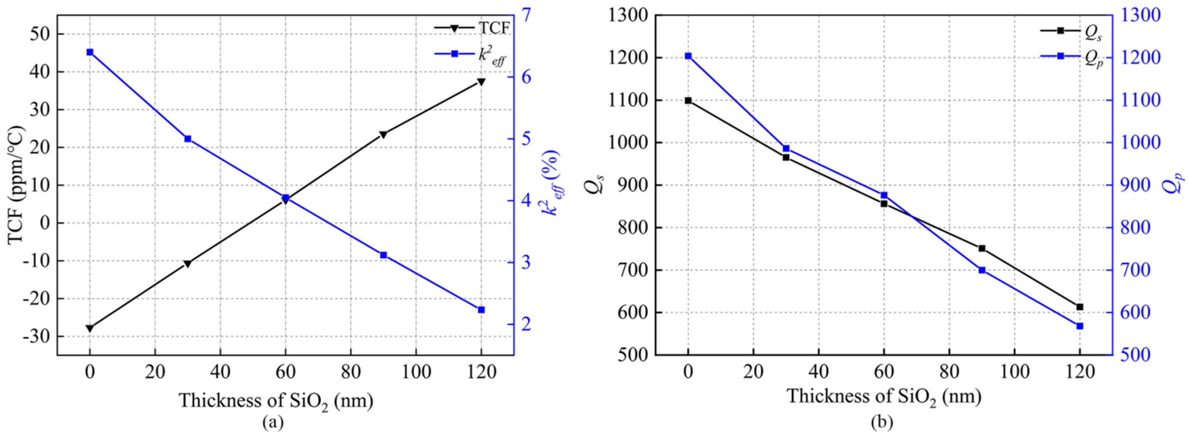

Figure 12. (**a**) Relationship between *TCF*, $k^2{}_{eff}$, and thickness of the SiO_2 film. (**b**) *Q* with different thicknesses.

A vector network analyzer (VNA) was used to test the electrical performance of the TC-FBAR, as shown in Figure 13. As shown in Figure 13a, the measurements achieved were f_0 = 2.492 GHz, BW_{3dB} = 15.02 MHz, *IL* = −3.1 dB, and out-of-band rejection of more than 40 dBc. The test and simulation results have consistent trends. However, compared to the simulation results, the measured insertion loss and the out-of-band suppression were slightly larger and smaller, respectively. During the fabrication, the Mo films may be oxidized to increase the insertion loss. The differences in the out-of-band rejection can be attributed to the electromagnetic parasitism that was not considered during encapsulation. Furthermore, the measured frequency was lower than the simulated frequency because of the deviations between the actual and designed film thicknesses. Figure 13b shows the temperature characteristic test curve of the TC-FBAR, which has a *TCF* of 0.8 ppm/°C at −55–125 °C. The test results were compared with different references, as shown in Table 1 [12–14,41–44]. From the comparison results, the lowest *TCF* and narrowest bandwidth were obtained in this work; thus, this resonator is suitable for fabricating a narrowband filter with a low *TCF*.

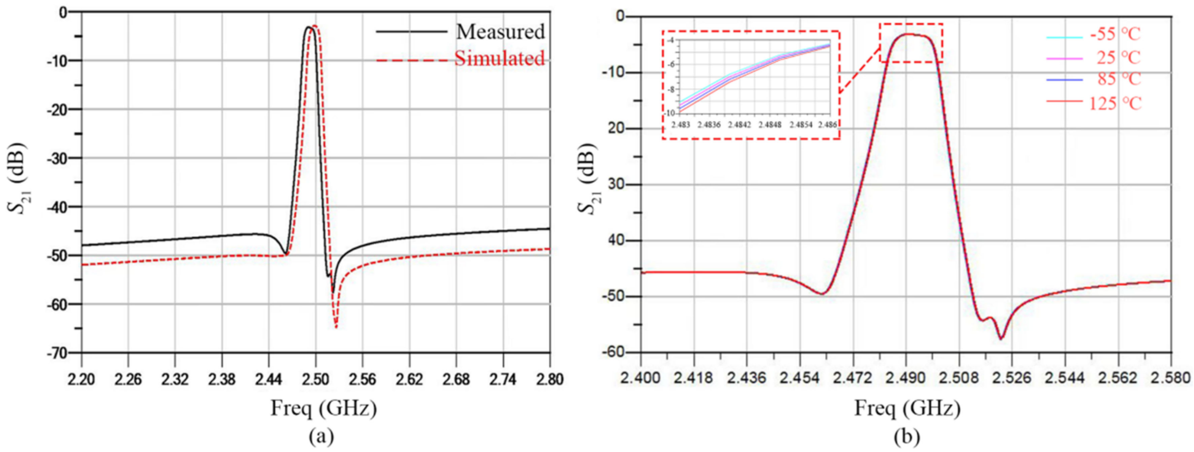

Figure 13. (**a**) Test and simulation comparison diagram of the TC-FBAR. (**b**) Frequency response diagram of the temperature characteristics of the TC-FBAR.

Table 1. Performance comparison.

Reference	f_0 (GHz)	IL (dB) (Within the Passband)	BW/3 dB (MHz)	*TCF* (ppm/°C) (−55–85 °C)
[12]	2.080	–	–	+1.5
[13]	1.320	–	–	±2.0
[14]	1.500	–	–	−6.0
[41]	3.723	2.40 (at f_0)	840.00	–
[42]	2.442	2.20	82.00	–
[43]	2.595	2.00	120.00	–
[44]	2.492	3.74	17.00	+5.0
This work	2.492	3.10	15.02	+0.8 (−55–125 °C)

4. Conclusions

In this study, a structural model of a TC-FBAR and its one-dimensional Mason model were established. ADS, HFSS, and COMSOL software were used to optimize the design of the TC-FBAR. Thus, a preparation method for the low-stress composite film was investigated. The principle of compressive- and tensile-stress-compensated effect was adopted to ensure that the stress of the composite film was within the required range. Moreover, the influence of the SiO_2 thickness on the temperature-compensated characteristics was studied. At a suitable SiO_2 thickness, the *TCF* could reach 0 ppm/°C. The TC-FBAR prepared by the cavity and composite film structures exhibited a low *TCF*.

Author Contributions: Y.L. provided the idea, designed the filter, implemented the simulation, and wrote the manuscript. K.S. and J.M. optimized the fabrication process, tested the devices, performed the theoretical analysis, and contributed to the manuscript preparation. Z.Y. provided theoretical guidance and revised the manuscript. Z.L. formulated the research issues and revised the manuscript. All authors have read and agreed to the published version of the manuscript.

Funding: This research was funded by the Core Electronic Devices, high-end universal chips and basic software products of China, 2017ZX01001201-002, and the Innovation Group Project of Sichuan Province (2022JDTD0018).

Institutional Review Board Statement: Not applicable.

Informed Consent Statement: Not applicable.

Data Availability Statement: Data sharing is not applicable to this article.

Acknowledgments: The authors would like to thank the editors and anonymous reviewers for their special effort.

Conflicts of Interest: The authors declare no conflict of interest.

References

1. Tsutsumi, J.; Iwaki, M.; Matsuda, T. Advanced Design Echnologies for SAW/FBAR Devices. In Proceedings of the International Symposium on Acoustic Wave Devices for Future Mobile Communication Systems, Keyaki Hall, Japan, 24–25 November 2015; pp. 84–90.
2. Du, B.; Lin, J.; Ou, L.; Shi, Y.; Ma, J. Full wave simulation and design of film bulk acoustic wave filters. In Proceedings of the International Conference on Electrical Engineering, Control and Robotics, Chengdu, China, 9 April 2018.
3. Fattinger, G.; Stokes, P.; Potdar, V.; Volatier, A.; Dumont, F.; Aigner, R. Miniaturization of BAW devices and the impact of wafer level packaging technology. In Proceedings of the IEEE International Ultrasonics Symposium (IUS), Prague, Czech Republic, 21–25 July 2013.
4. Heeren, W.; Fattinger, M.; Fattinger, G.; Volatier, A.; Aigner, R. Impact of thermo-mechanical stress on the TCF of WLP BAW filters. In Proceedings of the IEEE International Ultrasonics Symposium (IUS), Tours, France, 18–21 September 2016.
5. Zou, Q.; Bi, F.; Tsuzuki, G.; Bradley, P.; Ruby, R. Temperature-compensated FBAR duplexer for band 13. In Proceedings of the IEEE International Ultrasonics Symposium (IUS), Prague, Czech Republic, 21–25 July 2013.
6. Shin, J.; Song, I.; Kim, C.; Lee, M.; Son, S.; Kim, D.; Park, H.; Hwang, S.; Rieh, J. Balanced RF Duplexer with Low Interference Using Hybrid BAW Resonators for LTE Application. *ETRI J.* **2014**, *36*, 317–320. [CrossRef]
7. Tajic, A.; Aigner, R.; Aljoumayly, M.; Vetelino, F.; Fattinger, G. No-drift™ BAW-SMR: Over-moded reflector for temperature compensation. In Proceedings of the IEEE International Ultrasonics Symposium (IUS), Tours, France, 18–21 September 2016.
8. Warder, P.; Schnaufer, D. Temperature-Compensated Filter Technologies Solve Crowded Spectrum Challenges. *Microwave J.* **2014**, *57*, 92–96.
9. Farraro, R.; Mclellan, R. Temperature dependence of the Young's modulus and shear modulus of pure nickel, platinum, and molybdenum. *Metall. Trans. A* **1977**, *8*, 1563–1565. [CrossRef]
10. Pang, W.; Yu, H.; Zhang, H.; Kim, E. Temperature-compensated film bulk acoustic resonator above 2 GHz. *IEEE Electron Device Lett.* **2005**, *26*, 369–371. [CrossRef]
11. Tsubouchi, K.; Mikoshiba, N. Zero-temperature-coefficient SAW devices on AlN epitaxial films. *IEEE Trans. Sonics Ultrason.* **1985**, *32*, 634–644. [CrossRef]
12. Petit, D.; Abele, N.; Volatier, A.; Lefevre, A.; Ancey, P.; Carpentier, J. P0-15 Temperature Compensated Bulk Acoustic Wave Resonator and its Predictive 1D Acoustic Tool for RF Filtering. In Proceedings of the IEEE Ultrasonics Symposium (IUS), New York, NY, USA, 28–31 October 2007.
13. Bjurstrom, J.; Wingqvist, G.; Yantchev, V.; Katardjiev, I. Temperature compensation of liquid FBAR sensors. *J. Micromech. Microeng.* **2007**, *17*, 651–658. [CrossRef]
14. Qiang, Z.; Donald, L.; Frank, B.; Richard, R.; Martha, S.; Steve, O.; Yury, O.; Jyrki, K. High coupling coefficient Temperature compensated FBAR resonator for oscillator application with wide pulling range. In Proceedings of the IEEE International Frequency Control Symposium (IUS), Newport Beach, CA, USA, 1–4 June 2010.
15. Lakin, K.; McCarron, K.; McDonald, J. Temperature compensated bulk acoustic thin film resonators. In Proceedings of the IEEE Ultrasonics Symposium, San Juan, PR, USA, 22–25 October 2000.
16. Zhou, B.; Gao, Y.; He, Y. Simulation and Analysis of the Temperature-Compensated FBAR. *Appl. Mech. Mater.* **2015**, *720*, 490–495. [CrossRef]
17. Yamanouchi, K.; Hayama, S. SAW properties of SiO2/128°Y-X LiNbO3 structure fabricated by magnetron sputtering technique. *IEEE Trans. Sonics Ultrason.* **1984**, *31*, 51–57. [CrossRef]
18. Ruby. Resonator Device including Electrodes with Buried Temperature Compensated Layers. U.S. Patent 9479139B2, 25 October 2016. pp. 10–25.
19. Yu, H.; Pang, W.; Zhang, H.; Kim, E. Film bulk acoustic resonator at 4.4 GHz with ultra low temperature coefficient of resonant frequency. In Proceedings of the IEEE International Conference on Micro Electro Mechanical Systems, Miami Beach, FL, USA, 30 January–3 February 2005.
20. Yang, S.; Zhang, Y.; Sun, L.; Zhang, L.; Cheng, Z.; Wang, J.; Li, J. Study on AIN-based hybrid bulk acoustic wave resonator with low temperature coefficient of frequency. In Proceedings of the 13th China International Forum on Solid State Lighting: International Forum on Wide Bandgap Semiconductors China (SSLChina: IFWS), Beijing, China, 15–17 November 2016.
21. Allah, M.; Kaitila, J.; Thalhammer, R.; Weber, W.; Schmitt-Landsiedel, D. Temperature compensated solidly mounted bulk acoustic wave resonators with optimum piezoelectric coupling coefficient. In Proceedings of the IEEE International Electron Devices Meeting (IEDM), Baltimore, MD, USA, 7–9 December 2009.
22. Nishihara, T.; Taniguchi, S.; Ueda, M. Increased piezoelectric coupling factor in temperature-compensated film bulk acoustic resonators. In Proceedings of the IEEE International Ultrasonics Symposium (IUS), Taiwan, China, 21–24 October 2015.

23. Zou, Q.; Small, M.; Lee, D.; Bi, F.; Snyder, R.; Lamers, T.; Choy, J.; Ruby, R. Impact on film bulk acoustic resonator tempco and quality factor from boron doped SiO_2 temperature compensation material. In Proceedings of the 17th International Conference on Solid-State Sensors, Actuators and Microsystems (TRANSDUCERS & EUROSENSORS XXVII), Barcelona, Spain, 16–20 June 2013.
24. Larson, J.; Bradley, P.; Wartenberg, S.; Ruby, R. Modified Butterworth-Van Dyke circuit for FBAR resonators and automated measurement system. In Proceedings of the IEEE International Ultrasonics Symposium (IUS), San Juan, PR, USA, 22–25 October 2000.
25. Zhang, J.S.; Zhang, J.L.; Ning, Y. Study of SiO_2 Dielectric Film Stress Grownby the Method of Ion Assisted Deposition. *Chin. J. Lumin.* **2012**, *33*, 1304–1308. [CrossRef]
26. Alias, M.; Shaari, S.; Mitani, S. Optimization of electro-optical characteristics of Ga As-based oxide confinement VCSEL. *Laser Phys.* **2010**, *20*, 806–810. [CrossRef]
27. Alias, M.; Shaari, S.; Choudhury, P.; Mitani, S. Improved efficiency of Ga As-based VCSEL by utilizing fan-pad met allization and trench patterning. *Laser Phys.* **2009**, *19*, 2096–2101. [CrossRef]
28. Zhu, J.; Ding, W.; Wang, H.; Zhang, S.; Zhang, C.; Zhang, J.; Chai, W. Effect of Ar pressure on the properties of Mo films prepared by DC pulse magnetron sputtering. *Microfabr. Technol.* **2008**, *4*, 35–37.
29. Tian, B.; Xu, Y.; Cao, J.; Du, B. Influence of Dry Etching Conditions on Mo Sidewall Profile. *Piezoelectrics Acoustooptics* **2016**, *38*, 199–202.
30. Mortet, V.; Vasin, A.; Jouan, P.; Elmazria, O.; Djouadi, M. Aluminium nitride films deposition by reactive triode sputtering for surface acoustic wave device applications. *Surf. Coat. Technol.* **2003**, *176*, 88–92. [CrossRef]
31. Dimitrova, V.; Manova, D.; Paskova, T.; Uzunov, T.; Ivanov, N.; Dechev, D. Aluminium nitride thin films deposited by DC reactive magnetron sput tering. *Vacuum* **1998**, *2*, 161–164. [CrossRef]
32. Shen, Y.; Liu, Y.; Yang, H.; Duan, L.; Zhang, Y. Influence of the surface Roughness of $Mg_xZn_{1-x}O$ Piezoelectric Thin Films on Characteristics of the SMR. *Micronanoelectronic Technol.* **2014**, *51*, 776–779+784.
33. Gu, P.; Zheng, Z.; Zhao, Y.; Liu, X. Study on the Mechanism and Measurement of Stress of TiO_2 and SiO_2 Thin-films. *J. Phys.* **2006**, *55*, 6459–6463.
34. Sun, J.; Shi, X. Study of Internal Stress in PECVD SiO_2 Thin Films. *Semicond. Technol.* **2008**, *33*, 397–400.
35. Shin, H.; Song, J. Piezoelectric Coefficient Measurement of AlN Thin Films at the Nanometer Scale by Using Piezoresponse Force Microscopy. *J. Korean Phys. Soc.* **2010**, *2*, 580–585. [CrossRef]
36. Lueng, C.; Chan, H.; Fong, W.; Surya, C.; Choy, C. Piezoelectric Coefficient of Aluminum Nitride and Gallium nitride. *J. Appl. Phys.* **2000**, *9*, 5360–5363. [CrossRef]
37. Tonisch, K.; Cimalla, V.; Foerster, C.; Romanus, H.; Ambacher, O.; Dontsov, D. Piezoelectric Properties of Polycrystalline AlN Thin Films for MEMS Application. *Sens. Actuator A Phys.* **2006**, *132*, 658–663. [CrossRef]
38. Hu, N.; Zhang, Z.; Tao, J.; Zhou, C.; Zhang, H. Temperature Compensated Piezoelectric Bulk Acoustic Wave Filters. In Proceedings of the Symposium on Piezoelectricity, Acoustic Waves and Device Applications (SPAWDA), Shenzhen, China, 9–11 December 2011.
39. Lin, C.; Yen, T.; Lai, Y.; Felmetsger, V.; Hopcroft, A.; Kuypers, J.; Pisano, A. Temperature-Compensated Aluminum Nitride Lamb Wave Reso- nators. *IEEE Trans. Ultrason. Ferroelectr. Freq. Control* **2010**, *57*, 524–532. [CrossRef] [PubMed]
40. Matsuda, S.; Miura, M.; Matsuda, T.; Ueda, M.; Satoh, Y.; Hashimoto, K. Correlation between Fluorine-Doped SiO_2 Films properties and the propagation loss for Temperature Compensated SAW Devices. In Proceedings of the IEEE International Ultrasonics Symposium, Dresden, Germany, 7–10 October 2012.
41. Li, Q.; Li, X.; Xie, Y.; Cao, Z.; Dong, J. Synthesis of wideband bulk acoustic wave coupled resonator filter combined with lumped components. *Int. J. Circuit Theory Appl.* **2022**, *50*, 1907–1921. [CrossRef]
42. Tang, X.; Liu, Y.; Jiang, P.; Zhang, B. Design of a 2.4 GHz WiFI Band FBAR Bandpass Filter. *Piezoelectrics Acoustooptics* **2022**, *44*, 191–193+198.
43. Gu, J.; Wu, Y.; Lai, Z.; Wu, H. An N41-Band Bandpass BAW Filter Chip for Mobile Communications Based on FBARs. In Proceedings of the IEEE Asia-Pacific Microwave Conference (APMC), Hong Kong, Hong Kong, 8–11 December 2020; pp. 380–382.
44. Jia, Y.; Li, L.; Li, H. Development of S-Band Temperature-Compensated Narrow-Band FBAR Filter. *Semicond. Integr. Circuits* **2017**, *42*, 398–493.